Asymmetric Absorption in Acoustic Metamirror Based on Surface Impedance Engineering

Ailing Song,[1,2,*] Junfei Li,[2] Xiuyuan Peng,[2] Chen Shen,[2] Xiaohui Zhu,[2] Tianning Chen,[1,†] and Steven A. Cummer[2,‡]

[1] *School of Mechanical Engineering, Xi'an Jiaotong University, Xi'an, Shaanxi 710049, China*

[2] *Department of Electrical and Computer Engineering, Duke University, Durham, North Carolina 27708, USA*

(Received 27 June 2019; revised manuscript received 21 October 2019; published 20 November 2019)

Asymmetric wave manipulation has attracted growing interest due to its great importance in practical applications. We design and demonstrate a planar acoustic metamirror for realizing asymmetric sound absorption with a controllable retroreflection coefficient, which is absent in conventional lossless metasurfaces. We design the metamirror by realizing the required theoretical surface impedance profile, and then numerically and experimentally demonstrate its asymmetric response. The measured and simulated acoustic fields agree well with each other, which shows that the proposed metamirror can yield strongly asymmetric sound absorption: retroreflection and nearly full absorption for two opposite incident angles. In addition, the measured retroreflection coefficient and retroreflection angle are very close to the design values. We find that the asymmetrical excitation of evanescent waves plays a key role in the realization of asymmetric absorption. The proposed metamirror enriches the functionalities for acoustic wave manipulation and has prospective applications in many fields, such as acoustic antennas, acoustic sensing, and angle-encoded steganography.

DOI: 10.1103/PhysRevApplied.12.054048

I. INTRODUCTION

In recent years, wave manipulation and control has become a research focus in the field of acoustics and metamaterials have served as one of the primary methods used [1]. Metamaterials are artificially engineered structures with extraordinary properties stemming from local responses that lead to unprecedented functionalities. Two-dimensional metamaterials with planar or nearly planar shapes, so-called metasurfaces [2], have opened alternative possibilities to realize subwavelength-scale control of waves and achieve different functionalities including absorption [3], cloaking [4,5], focusing [6,7], and asymmetric wave manipulation [8].

The phenomenon of asymmetric acoustic wave manipulation has attracted growing interest due to its prospective applications in noise control [9], sound steering [10], and medical ultrasound imaging [11]. By asymmetrically manipulating acoustic waves, we can achieve different functionalities including asymmetric transmission [12–21], asymmetric reflection [22–29], asymmetric focusing [30,31], and asymmetric absorption [32–35]. Recent advances have demonstrated that the asymmetric control of transmitted waves can be achieved with various classes of structures, such as nonlinear materials [12–14], phononic crystals [15–17], grating structures [18], gradient-index structures [19], and acoustic metasurfaces [20,21]. Parity-time (*PT*) symmetric systems with balanced gain and loss can achieve unidirectional transparency at the exceptional points [22–24]. Unidirectional zero reflection can be realized in non-Hermitian acoustic systems by systematically synthesizing the exceptional points [25,26]. Apart from lossy systems, bianisotropic lossless metasurfaces with asymmetric reflection phase can be specifically designed to achieve scattering-free transmission [27,28]. Acoustic lossless bianisotropic gratings have been designed by optimizing the grating elements to achieve asymmetric transmission and reflection [29]. In addition, asymmetric acoustic focusing has been reported with passive *PT*-symmetric metamaterial crystal [30] and dual-layer metasurface [31].

This work is focused on asymmetric sound absorption structures, which only absorb acoustic waves coming from one particular direction. Asymmetric absorption with Helmholtz resonators [32,33] and hybrid membrane resonators [34,35] have been reported. However, the structures shown in this work are strictly one-dimensional propagation scenarios and extending the concept into two dimensions is not straightforward.

*ailingsong@outlook.com
†tnchen@mail.xjtu.edu.cn
‡cummer@ee.duke.edu

Moreover, these structures suffer from limited bandwidth since they are based on resonant structures. From the aspects of theory and practical applications, it is important to design planar structures with angle-dependent asymmetric absorption response, which have applications in various scenarios, such as acoustic antennas [36], acoustic sensing, and angle-encoded steganography [37] where directional responses are required. The possibilities of fabrication simplicity also make the planar structures more attractive in many applications. In the field of electromagnetics, the omega-type bianisotropic metasurface has been proposed to achieve resonant asymmetric absorption for illuminations from different sides [38]. Recently, angular-asymmetric absorption of electromagnetic waves was demonstrated via evanescent harmonics engineering [37]. However, in acoustics, the design and implementation of angular-asymmetric absorption structures has remained scarce. It was not until recently that a non-Hermitian planar metasurface realized angular-asymmetric absorption in acoustics at an exceptional point [39]. The achieved reflection coefficient (87% in simulation and 83% in experiment) is lower than the desired high theoretical value (over 97%), and the reflection coefficient is not easily controlled. Moreover, a pair of lossy and lossless resonators was used to obtain angle-dependent absorption based on resonance coupling [40], which makes this structure suffer from limited bandwidth. Therefore, it is necessary to explore alternative methods to realize angle-dependent asymmetric absorption with improved performance.

In this paper, we design and demonstrate a planar acoustic metamirror capable of realizing asymmetric absorption with a controllable retroreflection coefficient. The proposed metamirror greatly enriches the functionalities for acoustic wave manipulation and the systematic design method based on surface impedance engineering may also be applied to other applications. First, we perform a theoretical analysis showing that the asymmetrical excitation of evanescent waves is required for the realization of asymmetric absorption at two opposite incident angles. Next, periodically arranged channels loaded with foam are proposed to precisely realize the required surface impedance profile by tuning the heights of the air cavity and foam. The metamirror design is further verified by numerical simulations and experimental measurements. The experimental results show good agreement with the simulation results and both results show that the proposed metamirror with specifically engineered surface impedance exhibits retroreflection and total absorption for acoustic waves coming from opposite incident angles. This metamirror can be designed to have a specific retroreflection coefficient by realizing the corresponding surface impedance profile, which is a distinct feature compared with previously reported work.

II. THEORY AND DESIGN

A. Theoretical analysis

The schematic of the asymmetric absorbing metamirror is shown in Fig. 1, where a metamirror with periodicity D extends in the x direction and the incident angle is θ_i. When the acoustic waves impinge upon the metamirror, it exhibits asymmetric absorption dependent on the incident angle: controllable retroreflection for $\theta_i = +\theta$ and full absorption for $\theta_i = -\theta$. The acoustic waves incident from opposite angles are reflected into different diffracted orders with different amplitudes, so the absorptance is not an even function of angle. The x component of the wave number for the nth diffracted wave is $k_{rx} = k_0 \sin\theta_i + 2\pi n/D$, where k_0 is the wave number of air in free space and n is the diffracted order. For k_{rx} with different n, if $|k_{rx}| < k_0$, it corresponds to a propagating wave, while if $|k_{rx}| > k_0$, it is evanescent and does not contribute to the far field. When acoustic waves impinge on the metamirror at an angle of θ_i, the incident field is

$$p_{i1,2}(x,z) = p_0 e^{-jk_x x} e^{-jk_z z}, \tag{1}$$

where p_0 is the amplitude of the incident wave, $k_x = k_0 \sin\theta_i$ is the x component of the incident wave number, and $k_z = -k_0 \cos\theta_i$ is the z component of the incident wave number. The reflected field scattered by the periodically modulated metamirror can be represented as a sum of diffracted orders as

$$p_{r1,2}(x,z) = \sum_{n=-\infty}^{+\infty} A_n e^{-jk_{rx}x} e^{-jk_{rz}z}, \tag{2}$$

where A_n is the amplitude of the nth diffracted wave and k_{rx} and k_{rz} are the x and z components of the wave number for the nth diffracted wave, respectively.

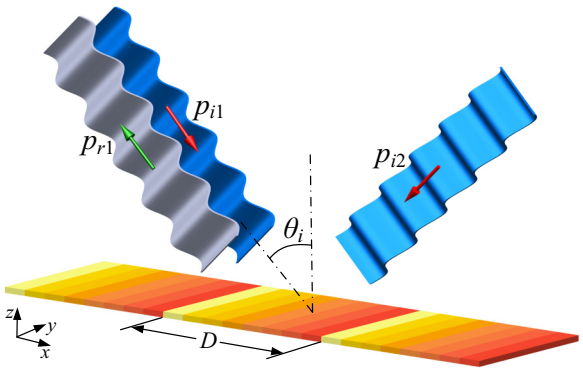

FIG. 1. Schematic of the asymmetric absorbing metamirror. The red and green arrows indicate the incident waves and the reflected waves, respectively.

For the incident angle of $\theta_i = +\theta$, we require that the reflected acoustic field is constituted only by one propagating diffracted wave $n = -1$ (corresponding to the retroreflection). The amplitudes of the specular reflected wave and evanescent waves are zero, as shown in the top panel of Fig. 2(a). Therefore, the x component of the wave number for $n = -1$ diffracted wave ($k_{rx(n=-1)} = k_0 \sin\theta_i - 2\pi/D$) is equal to $-k_0 \sin\theta_i$, thus we can see that the periodicity of the metamirror is $D = \lambda_0/(2\sin\theta_i)$, where λ_0 is the wavelength in air [41]. The retroreflected sound pressure is

$$p_{r1}(x,z) = r_1 p_0 e^{j k_x x} e^{j k_z z}, \tag{3}$$

where r_1 is the controllable retroreflection coefficient of the $n = -1$ diffracted order. The total sound pressure at $z = 0$ is

$$p_{t1}(x,0) = p_0 e^{-j k_x x} + r_1 p_0 e^{j k_x x}. \tag{4}$$

The corresponding normal velocity at $z = 0$ is

$$-\hat{n}\cdot\vec{v}_{t1}(x,0) = \frac{p_0\cos\theta_i}{Z_0}(e^{-j k_x x} - r_1 e^{j k_x x}), \tag{5}$$

where $\hat{n}$ is the unit vector normal to the metamirror, $\vec{v}_{t1}$ is the total velocity vector, and Z_0 is the characteristic impedance of air. Equations (4) and (5) are used to define the required surface impedance profile of this metamirror, which is written as

$$Z_s = \frac{Z_0(1-r_1^2)}{[1+r_1^2-2r_1\cos(2k_x x)]\cos\theta_i} + j\frac{2Z_0 r_1 \sin(2k_x x)}{[1+r_1^2-2r_1\cos(2k_x x)]\cos\theta_i}. \tag{6}$$

The surface impedance defined by Eq. (6) is a complex number. The real part in Eq. (6) remains positive for a passive metamirror and is an even function of x. In contrast, the imaginary part in Eq. (6) is an odd function of x, which can create an angle-dependent asymmetric effect for acoustic waves.

When the metamirror defined by Eq. (6) is illuminated by acoustic waves at an angle of $\theta_i = -\theta$, total absorption is realized, as shown in the bottom panel of Fig. 2(a). As the phase distribution of the incident field is reversed, it is possible to fulfill the boundary condition only if some evanescent waves are excited in this case. The amplitudes of diffracted waves for specular reflection ($n = 0$) and retroreflection ($n = +1$) are zero. So the total reflected acoustic field is constituted by a set of evanescent waves. The total sound pressure at $z = 0$ is

$$p_{t2}(x,0) = p_0 e^{-j k_x x} + \sum_{n=-\infty}^{+\infty} A_n e^{-j k_{rx} x}. \tag{7}$$

The corresponding normal velocity at $z = 0$ is

$$-\hat{n}\cdot\vec{v}_{t2}(x,0) = \frac{p_0\cos\theta_i}{Z_0}e^{-j k_x x} - \sum_{n=-\infty}^{+\infty} A_n \frac{k_{rz}}{\rho\omega} e^{-j k_{rx} x}, \tag{8}$$

where $\vec{v}_{t2}$ is the total velocity vector, ρ is the air density, and ω is the angular frequency. By enforcing the boundary condition

$$\frac{p_{t2}(x,0)}{-\hat{n}\cdot\vec{v}_{t2}(x,0)} = Z_s. \tag{9}$$

The amplitudes of different diffracted orders can be determined.

As an example, the metamirror is designed at 3000 Hz and $\theta = 45°$ in this paper, and the periodicity of the metamirror is $D = 80.8$ mm, which is a subwavelength. It is noted that the relationship between the wavelength and the unit cell periodicity D is affected by the designed incident angle and the analysis is always effective if all the diffracted waves are evanescent for the incident angle of $\theta_i = -\theta$. The surface impedance profile is determined by the retroreflection coefficient r_1, which is controllable and can be arbitrary values between 0 and 1. Here, we pick three values for demonstration: $r_1 = 0.99$, $r_1 = 0.70$, and $r_1 = 0.40$. For the incident angle of $\theta_i = +45°$, the amplitudes of the diffracted waves are shown in Fig. 2(b) and we can see that only one diffracted order of $n = -1$ produces a propagating wave, which corresponds to retroreflection. The retroreflection coefficients of the $n = -1$ diffracted order agree well with the defined values. The amplitudes of all the other diffracted waves are zero, as expected. Figure 2(c) shows the amplitudes of the diffracted waves when the incident angle is $\theta_i = -45°$. The amplitudes of the propagating waves $n = 0$ (specular reflection) and $n = +1$ (retroreflection) are always zero for the three retroreflection coefficients. The diffracted orders of all excited waves are negative, which correspond to the evanescent waves. Hence all the incident energy can be dissipated in the metamirror to ensure total absorption. It is noted that the higher retroreflection coefficient we set for the $\theta_i = +45°$ case, the stronger the evanescent waves that will be excited in the $\theta_i = -45°$ case to ensure total absorption. Total absorption in this direction is attributed to the proper excitation of a set of evanescent waves propagating along the $-x$ direction. From the above analysis, we can conclude that asymmetric absorption can be realized by asymmetrically exciting the evanescent waves for opposite incident angles.

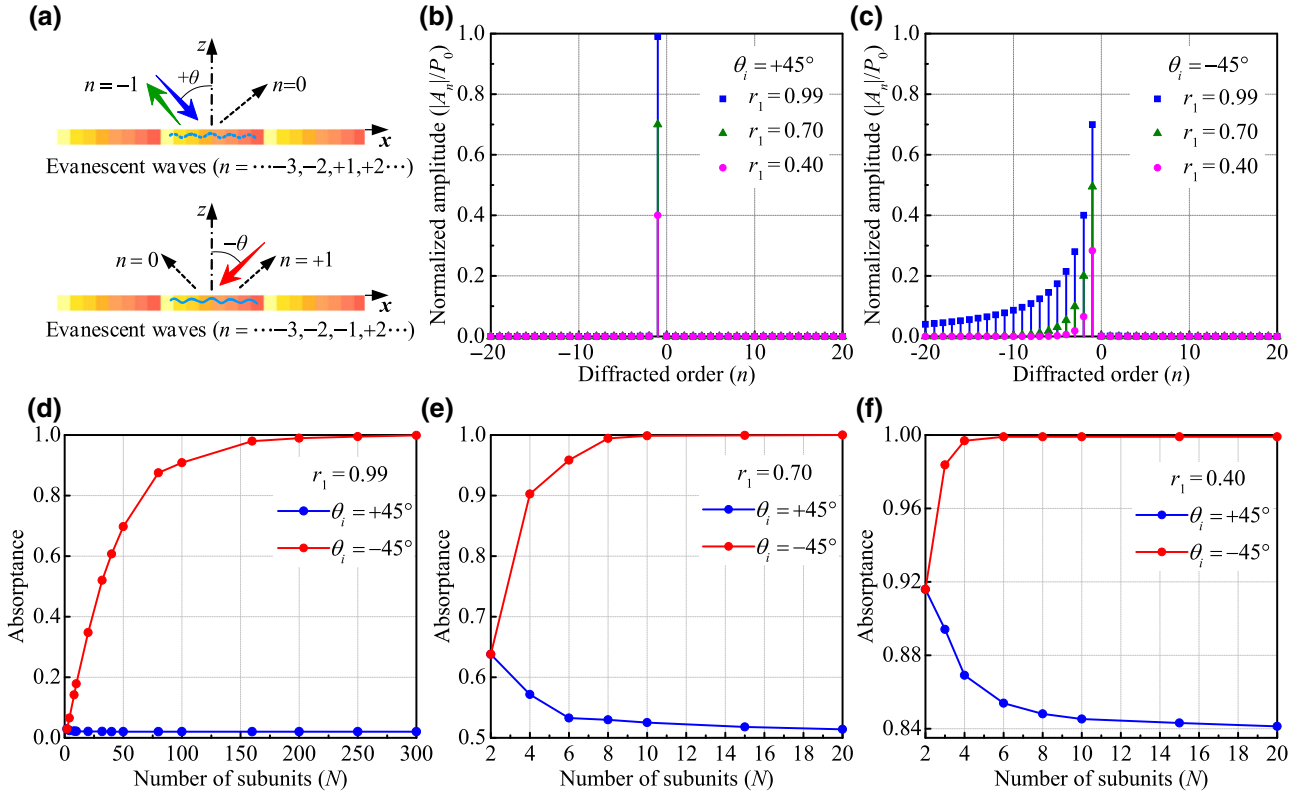

FIG. 2. (a) Illustration of the asymmetric absorption performance of the proposed metamirror when the incident angles are $+\theta$ (top panel) and $-\theta$ (bottom panel). Normalized amplitudes of different diffracted waves for three different retroreflection coefficients when the incident angles are (b) $\theta_i = +45°$ and (c) $\theta_i = -45°$. Calculated absorptance versus the number of subunits N in one period when the surface impedance is determined by the retroreflection coefficients of (d) $r_1 = 0.99$, (e) $r_1 = 0.70$, and (f) $r_1 = 0.40$.

In practical realization, the number of subunits in one period is finite and the surface impedance is discrete. Therefore, it is necessary to study the effect of the discretization resolution on the asymmetric absorption effect. We calculate the absorptance as a function of the number of subunits N in one period for $\theta_i = +45°$ and $\theta_i = -45°$. A stepwise constant function with N steps in one period is used to model the discrete surface impedance. Figures 2(d)–2(f) show the change of absorptance as the discretization changes when the surface impedance profile is determined by three retroreflection coefficients $r_1 = 0.99$, $r_1 = 0.70$, and $r_1 = 0.40$, respectively. It is observed that the asymmetry of absorption is strongly dependent on the number of subunits. When the metamirror only contains two subunits in one period, the absorptance for $\theta_i = +45°$ equals that for $\theta_i = -45°$, which is a consequence of the symmetry of the metamirror. For the incident angle of $\theta_i = -45°$, the absorptance gradually increases and approaches the design value with the increase of the number of subunits. For the metamirror designed with a larger retroreflection coefficient, more subunits are needed in one period to ensure the excitation of evanescent waves for total absorption in the $\theta_i = -45°$ case. For example, to achieve asymmetric absorption in the metamirror designed by $r_1 = 0.99$, more than 150 subunits should be included in one period.

In our realization, the surface impedance profile is determined by $r_1 = 0.70$ and each period is discretized into eight subunits. To validate that such a discretization is enough to achieve asymmetric sound absorption, we perform simulations using the pressure acoustics module in COMSOL Multiphysics software based on the finite element method (FEM). The metamirror is modeled by the impedance boundary conditions [42], and the impedance values of each subunit are directly set to the required discrete surface impedance. A Gaussian beam of 3000 Hz impinges on the metamirror with opposite incident angles. The incident and scattered field distributions at the incident angles of $\theta_i = +45°$ and $\theta_i = -45°$ are shown in Figs. 3(a) and 3(b), respectively. The simulated acoustic fields indicate that the metamirror with eight subunits in one period can realize the desired asymmetric absorption response: retroreflection with the retroreflection coefficient of 0.698 for $\theta_i = +45°$, and nearly total absorption with an absorptance of 99.6% for $\theta_i = -45°$. Therefore, it can be concluded that good asymmetric absorption performance can be achieved in such discretization. In principle, the metamirror for other arbitrary retroreflection coefficients

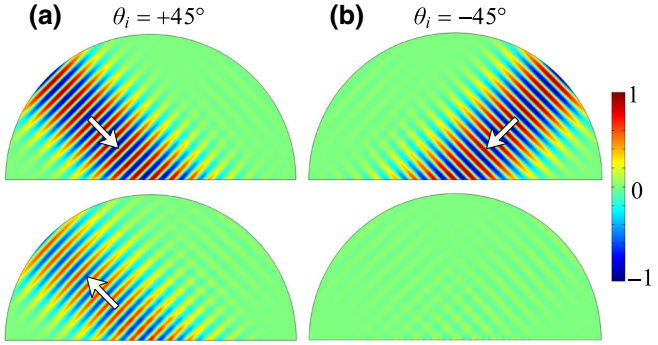

FIG. 3. Simulated incident (top panel) and scattered (bottom panel) acoustic fields by using the impedance model when the incident angles are (a) $\theta_i = +45°$ and (b) $\theta_i = -45°$. The white arrows denote the propagation directions of acoustic waves.

between 0 and 1 can also be achieved by realizing the corresponding surface impedance profile.

B. Realization of the required surface impedance profile

To physically implement the designed metamirror, we realize the required surface impedance profile using the periodically arranged channels loaded with foam, as shown in Fig. 4(a). The subunit numbers are labeled as $S1$, $S2$,..., $S7$, $S8$. By tuning the air height h_0 and the foam height h_1, this structure can provide the required real and imaginary parts of the surface impedance. The periodicity of the metamirror is $D = 80.8$ mm, the subunit width is $d = 10.1$ mm. The subunits are separated by walls with a thickness of 0.6 mm, which yield the channels with a width of $d_0 = 9.5$ mm. Next, h_0 and h_1 for each subunit need to be determined. The subunit shown in Fig. 4(a) can be analyzed with the transfer matrix, which is defined as [43]

$$\begin{bmatrix} p_0 \\ -\hat{n}\cdot\vec{v}_0 \end{bmatrix} = \begin{bmatrix} T_{11} & T_{12} \\ T_{21} & T_{22} \end{bmatrix} \begin{bmatrix} p_1 \\ -\hat{n}\cdot\vec{v}_1 \end{bmatrix}, \tag{10}$$

where p_0 and p_1 are the pressure amplitude at the upper and bottom ends of the subunit, respectively. $\vec{v}_0$ and $\vec{v}_1$ are the velocity vectors at the upper and bottom ends of the subunit, respectively. The total transmission matrix of the subunit is expressed as

$$T = \begin{bmatrix} T_{11} & T_{12} \\ T_{21} & T_{22} \end{bmatrix} = T_{\text{air}} T_{\text{foam}}, \tag{11}$$

where T_{air} and T_{foam} are the transmission matrices of the air cavity and foam, respectively. They are given as

$$T_{\text{air, foam}} = \begin{bmatrix} \cos(k_{0,1}h_{0,1}) & jZ_{0,1}\sin(k_{0,1}h_{0,1}) \\ j\frac{\sin(k_{0,1}h_{0,1})}{Z_{0,1}} & \cos(k_{0,1}h_{0,1}) \end{bmatrix}, \tag{12}$$

where Z_0, k_0 and Z_1, k_1 are the characteristic impedances and wave numbers of air and foam, respectively. By substituting Eq. (12) into Eq. (11), four elements of the total transmission matrix can be obtained. The normal velocity at the bottom end of the subunit $-\hat{n}\cdot\vec{v}_1$ is zero, so the pressure amplitude and the normal velocity at the upper end of the subunit are

$$p_0 = T_{11}p_1, \tag{13}$$

$$-\hat{n}\cdot\vec{v}_0 = T_{21}p_1. \tag{14}$$

Equations (13) and (14) define the impedance at the upper end of the subunit as

$$Z_u{}' = \frac{jZ_0[Z_0\sin(k_0h_0)\sin(k_1h_1) - Z_1\cos(k_0h_0)\cos(k_1h_1)]}{[Z_1\sin(k_0h_0)\cos(k_1h_1) + Z_0\cos(k_0h_0)\sin(k_1h_1)]}. \tag{15}$$

Considering the thickness of the hard walls between adjacent subunits, the impedance at the upper end of the subunit becomes

$$Z_u = Z_u{}'\frac{d}{d_0}. \tag{16}$$

By matching the surface impedance of each subunit in Eq. (16) with the impedance requirement from Eq. (6), we can obtain the heights of the air cavity and foam with given parameters k_0, k_1, Z_0, and Z_1.

The parameters of air and foam are measured in the experiment with the four-microphone method [44] and the experimental setup is shown in Fig. 4(b). The parameters are measured in an impedance tube (BSWA SW477) with an inner diameter of 30 mm. A loudspeaker placed at one end of the impedance tube is used to generate sinusoidal signals. A PA50 power amplifier is used to drive the loudspeaker. The other end of the impedance tube is an anechoic termination to avoid reflections. The sound pressures at four locations are measured by four BSWA ¼ in. microphones MPA416, which are directly connected to 4-channel MC3242 data acquisition hardware. The one-load method is used to calculate the material parameters by taking advantage of the homogeneous and isotropic material. First, the air parameters are measured and the measured wave number of air at 3000 Hz is $k_0 = (54.79 - 0.32i)$ rad/m and the measured characteristic impedance of air at 3000 Hz is $Z_0 = (412.27 - 10.83i)$ Pa·s/m. Then the foam cylinder is placed in the right side of the sample holder to measure the foam parameters, as shown in the inset of Fig. 4(b). Figures 4(c) and 4(d) show the measured wave number and characteristic impedance of the foam from 2600 to 3600 Hz, respectively. Both the wave number and characteristic impedance have complex values and are dispersive. At 3000 Hz, the measured

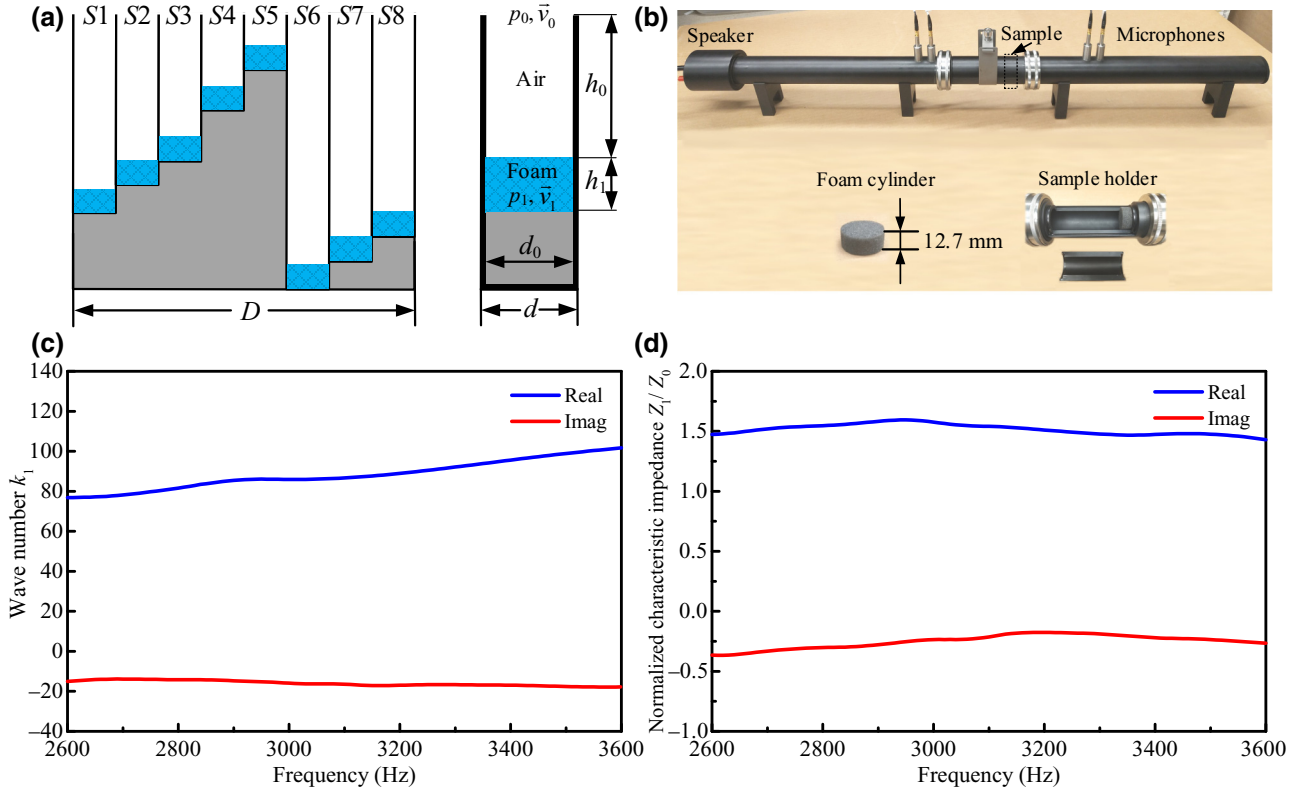

FIG. 4. (a) Schematic of the asymmetric absorbing metamirror composed of periodically arranged channels loaded with foam. The heights of the air cavity and foam for each subunit are different to obtain the required surface impedance. (b) Experimental setup for foam parameters' measurement by using the four-microphone method. The dashed box represents the position of the sample. The inset shows the foam cylinder and how it is positioned inside the sample tube. (c) Measured wave number of the foam. (d) Measured normalized characteristic impedance of the foam.

wave number of the foam is $k_1 = (85.91 - 15.92i)$ rad/m and the measured characteristic impedance of the foam is $Z_1 = 412.27(1.58 - 0.26i)$ Pa·s/m.

Based on the measured parameters and Eq. (16), the real and imaginary parts of the surface impedance against the air height and foam height are obtained, as shown in Fig. 5(a). The real parts of the surface impedance are always positive, indicating the subunits are lossy. The imaginary parts of the surface impedance represent the phase change in the subunit. The required surface

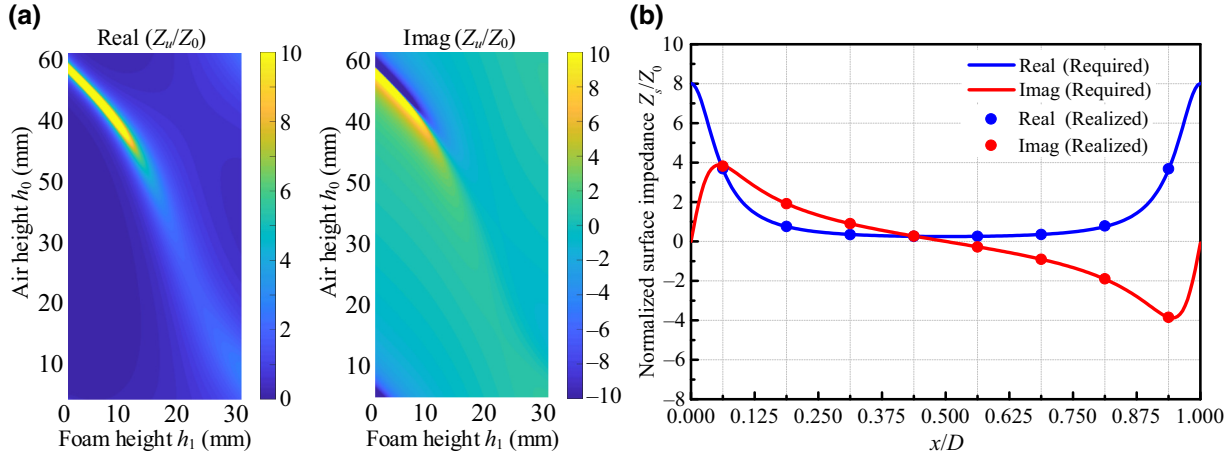

FIG. 5 (a) Real (left panel) and imaginary (right panel) parts of the surface impedance as functions of air height h_0 and foam height h_1. (b) Required and realized surface impedance in one period when $r_1 = 0.70$.

TABLE I. The design parameters for each subunit at 3000 Hz.

Design parameters	*S*1	*S*2	*S*3	*S*4	*S*5	*S*6	*S*7	*S*8
h_0 (mm)	40.7	34.0	25.6	15.2	5.5	56.5	50.8	46.2
h_1 (mm)	11.8	12.4	13.3	14.3	14.3	13.1	12.4	11.7

impedance profile defining the metamirror based on Eq. (6) is shown in Fig. 5(b) (blue and red lines), which shows the real part is an even function and the imaginary part is an odd function. In our realization, the required discrete surface impedance can be expressed as Z_s (x_m), where $x_m = D(0.5 + m)/N$ is the central point of the subunit, $m = 0, 1,\ldots, 7$ and $N = 8$. By combining the discrete surface impedance and Fig. 5(a), the air height and foam height for each subunit can be obtained and the design parameters are given in Table I. Based on the measured material parameters and the geometrical parameters, we perform numerical simulations and obtain the realized surface impedance for each subunit as marked by blue and red dots in Fig. 5(b), which agree well with the theoretical curves.

III. SIMULATIONS AND EXPERIMENTS

The metamirror design is then verified with numerical simulations and experiments. The simulations are performed in COMSOL Multiphysics software and the left and right boundaries are perfectly matched layers (PMLs) to reduce reflections. The experimental setup and four periods of the fabricated sample are shown in Fig. 6(a). The grooved structure is fabricated with fused deposition modeling three-dimensional (3D) printing technology using acrylonitrile butadiene styrene (ABS) plastic with a density of 1180 kg/m^3 and a sound speed of 2700 m/s. The walls of the metamirror are 0.6 mm in thickness and can be considered as acoustically rigid as their characteristic impedance is much larger than that of air. The fabricated metamirror consists of 13 periods, and the overall size is 105.04 cm (length) by 7.1 cm (thickness) by 4.0 cm (height). The sample is placed in a two-dimensional (2D) waveguide with a height of 4.0 cm to ensure 2D acoustic wave propagation. Sound-absorbing foams are used to absorb the incoming waves at boundaries. To generate the required Gaussian beam, 28 speakers (PUI AS07104PO-R) are used to assemble a liner speaker array and each speaker sends a short Gaussian-modulated sinusoidal pulse. All the speakers are synchronized by a 32-channel analog output device (NI PCI-6723) with different phases and amplitudes, so we can obtain a spatially modulated Gaussian beam with a certain incident angle. In the scan area, the signals at each position are recorded by a moving microphone (ADMP401) with a step of 1 cm and averaged four times to reduce noise. The received signals at different positions are then time windowed to eliminate the unavoidable boundary reflections and the acoustic fields are calculated by performing Fourier transform of the time-domain signals [45–47]. The incident and total acoustic fields are measured without and with the metamirror, respectively. The scattered field is obtained by subtracting the incident field from the total field.

To demonstrate the performance of the proposed metamirror, energy distributions at different directions are first investigated. The normalized amplitudes of the reflected waves are calculated by performing spatial Fourier transform along a line 1 cm away from the metamirror and the simulated and measured results are shown in Fig. 6(b). At the operating frequency of 3000 Hz, the measured results show good agreement with the simulated ones. For the incident angle of $\theta_i = +45°$, we can clearly see that almost all the reflected energy concentrates in the desired direction (retroreflection direction) and the amplitudes of other diffracted waves are very small. The simulated and measured retroreflection coefficients r_1 are 0.692 and 0.697, which are very close to the design value of 0.70. The corresponding retroreflection angles in simulation and experiment are 44.8° and 45.6°, respectively. For the incident angle of $\theta_i = -45°$, the amplitudes always remain at nearly zero, and the simulated and measured absorptances are 98.7% and 98.3%, respectively. The energy distributions indicate that the metamirror can yield asymmetric absorption response for two opposite incident angles.

To further evaluate the performance of asymmetric absorption of the metamirror, the incident and scattered acoustic fields are simulated and measured, as shown in Figs. 6(c) and 6(d). A Gaussian beam impinges on the metamirror with opposite incident angles. The areas marked by the red boxes in the top panel are scanned by the moving microphone. The top and bottom panels represent the simulated and measured acoustic fields, respectively. Excellent agreement can be observed between the simulated and measured fields, confirming the desired asymmetric absorption response. For the incident angle of $\theta_i = +45°$, the incident waves are reflected to the original incident direction with smaller amplitude and only retroreflection occurs, as shown in Fig. 6(c). For the incident angle of $\theta_i = -45°$, no scattered field distribution is observed, which means all the incident energy is absorbed by the metamirror, as shown in Fig. 6(d).

To quantitatively investigate the spectral performance of the proposed metamirror, the absorptance in simulations and experiments are calculated, and the results within the frequency range from 2600 to 3600 Hz are shown in Fig. 7 showing differences in absorptance between two opposite incident angles. We perform spatial Fourier transform of the sound pressure along a line 1 cm away from the metamirror and obtain the amplitudes of all Fourier components. Then the energy distributions associated with

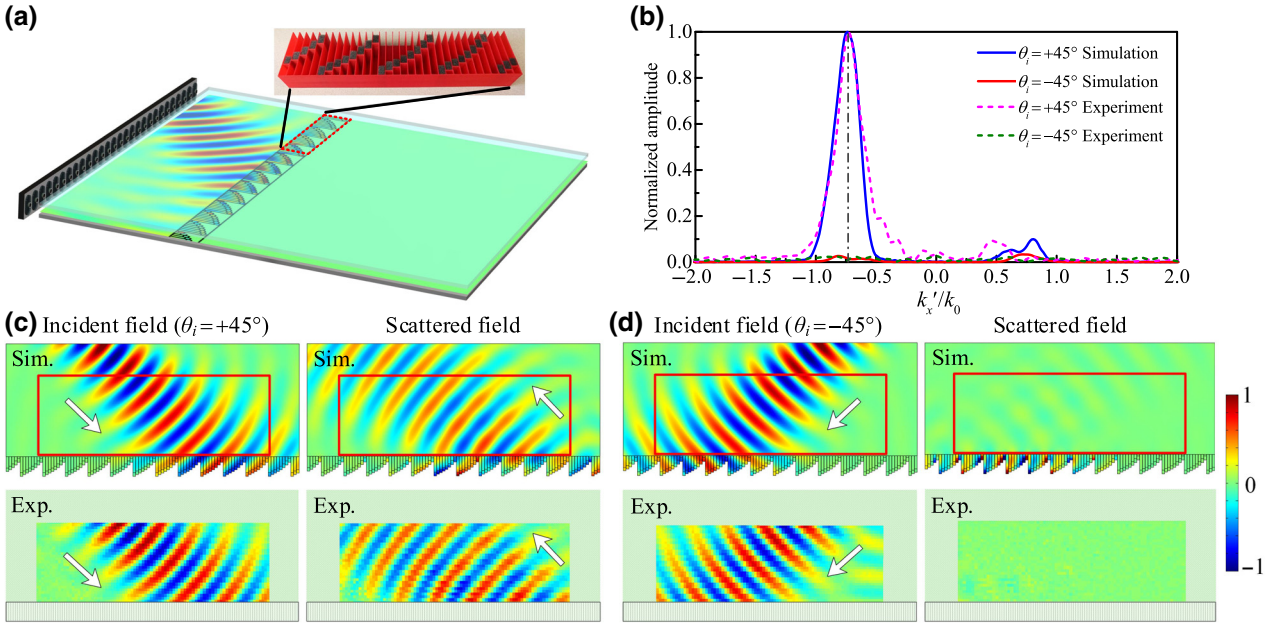

FIG. 6. (a) Schematic representation of the experimental setup and the photograph of the fabricated sample with four periods. (b) Normalized amplitude of the reflected waves on different directions along the line 1 cm away from the metamirror. (c) Incident (left panel) and scattered (right panel) acoustic fields in simulations and experiments at $\theta_i = +45°$. (d) Incident (left panel) and scattered (right panel) acoustic fields in simulations and experiments at $\theta_i = -45°$. The top and bottom panels represent the simulated and measured acoustic fields at 3000 Hz, respectively. The white arrows denote the propagation directions of acoustic waves.

different k_x' (x component of the wave number) are obtained. If $|k_x'|$ is larger than k_0, the y component of the wave number k_y' becomes imaginary due to the relation $|k_x'|^2 + |k_y'|^2 = k_0^2$. Therefore, this diffracted wave is an evanescent wave and does not contribute to the far field. By integrating the acoustic power of all the propagating waves corresponding to $|k_x'| < k_0$, we can obtain the incident power P_i and the total reflected power P_r, so the absorptance of the metamirror can be obtained $a = 1 - P_r / P_i$. It should be noted that only the power of the propagating waves is considered when we calculate the reflected power. For the incident angle of $\theta_i = -45°$, the simulated and measured absorptances agree well with each other and the absorptance is always above 92% (corresponds to the absorption rate of larger than 11 dB), which indicates the metamirror has a moderate absorptance at the frequency near the designed frequency. For the incident angle of $\theta_i = +45°$, the variation tendency of the measured absorptance is consistent with that of the simulated one: the absorptance first decreases and then increases as the frequency increases. This can be explained as the required surface impedance cannot be preserved when the working frequency is far away from the designed frequency. There are small deviations between the simulated and measured results in the $\theta_i = +45°$ case, which may be caused by several factors. The surface roughness of the fabricated sample and the narrow channel make the loss of air in experiments slightly larger than that in simulations. The fabrication errors of the grooved structure and the cutting errors of the foam slices may result in the deviation of the surface impedance from the required values. The imperfect absorbing boundaries in the waveguide can also cause some unwanted reflections from the boundaries. Although

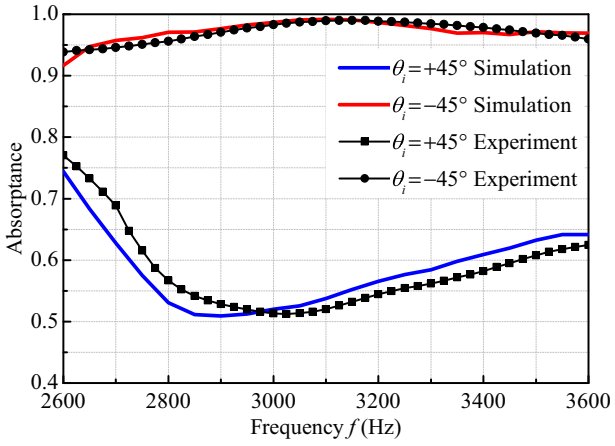

FIG. 7. Numerically calculated and experimentally measured absorptance at different frequencies for opposite incident angles. Blue and red lines represent the simulated absorptances at $\theta_i = +45°$ and $\theta_i = -45°$, respectively. Black squares and black dots represent the measured absorptance at $\theta_i = +45°$ and $\theta_i = -45°$, respectively.

the current metamirror is designed at 3000 Hz, asymmetric absorption behavior is also observed at other frequencies, which ensures the effectiveness of the proposed metamirror at the frequency near the designed frequency.

IV. CONCLUSIONS

In summary, we theoretically design and experimentally demonstrate an acoustic metamirror capable of realizing asymmetric absorption response with a controllable retroreflection coefficient. The design approach is based on precise control of the surface acoustic impedance profile of the metamirror. The metamirror is composed of periodically arranged channels loaded with foam, and the surface acoustic impedance profile can be engineered by tuning the heights of the air cavity and foam. The measured results are in good agreement with the simulated results, showing that the proposed metamirror exhibits an asymmetric absorption performance created by the asymmetrical excitation of the evanescent waves. In principle, the metamirror for other arbitrary retroreflection coefficients between 0 and 1 can also be fulfilled by realizing the corresponding surface impedance profile. The design method of wave manipulation via surface impedance engineering may also be applied to other applications, such as acoustic focusing [6,7], acoustic carpet cloaking [48,49], sound steering [10], and so on. The angle-dependent asymmetric absorption concept enriches the functionalities for acoustic wave manipulation and has some potential applications in many fields, such as acoustic antennas, acoustic sensing, and angle-encoded steganography. In addition, this distinctive behavior that cannot be realized in conventional lossless metasurfaces can greatly expand the family of acoustic metasurfaces.

ACKNOWLEDGMENTS

This work was supported by a Multidisciplinary University Research Initiative grant from the Office of Naval Research (Grant No. N00014-13-1-0631), an Emerging Frontiers in Research and Innovation grant from the National Science Foundation (Grant No. 1641084), and National Natural Science Foundation of China (Grant No. 51675402). A. L. S. also acknowledges the scholarship from the Chinese Scholarship Council (Grant No. 201806280160).

[1] Y. D. Xu, Y. Y. Fu, and H. Y. Chen, Planar gradient metamaterials, Nat. Rev. Mat. **1**, 16067 (2016).
[2] B. Assouar, B. Liang, Y. Wu, Y. Li, J. C. Cheng, and Y. Jing, Acoustic metasurfaces, Nat. Rev. Mat. **3**, 460 (2018).
[3] C. Shen and S. A. Cummer, Harnessing Multiple Internal Reflections to Design Highly Absorptive Acoustic Metasurfaces, Phys. Rev. Appl. **9**, 054009 (2018).
[4] H. Esfahlani, S. Karkar, and H. Lissek, Acoustic carpet cloak based on an ultrathin metasurface, Phys. Rev. B **94**, 014302 (2016).
[5] C. Faure, O. Richoux, S. Felix, and V. Pagneux, Experiments on metasurface carpet cloaking for audible acoustics, Appl. Phys. Lett. **108**, 064103 (2016).
[6] J. Chen, J. Xiao, D. Lisevych, A. Shakouri, and Z. Fan, Deep-subwavelength control of acoustic waves in an ultra-compact metasurface lens, Nat. Commun. **9**, 4920 (2018).
[7] S. D. Zhao, A. L. Chen, Y. S. Wang, and C. Z. Zhang, Continuously Tunable Acoustic Metasurface for Transmitted Wavefront Modulation, Phys. Rev. Appl. **10**, 054066 (2018).
[8] Y. Li, C. Shen, Y. B. Xie, J. F. Li, W. Q. Wang, S. A. Cummer, and Y. Jing, Tunable Asymmetric Transmission via Lossy Acoustic Metasurfaces, Phys. Rev. Lett. **119**, 035501 (2017).
[9] S. A. Cummer, Selecting the direction of sound transmission, Science **343**, 495 (2014).
[10] P. Zhang, T. C. Li, J. Zhu, X. F. Zhu, S. Yang, Y. Wang, X. B. Yin, and X. Zhang, Generation of acoustic self-bending and bottle beams by phase engineering, Nat. Commun. **5**, 4316 (2014).
[11] D. Monroe, One-way mirror for sound waves, Phys. Rev. Focus **24**, 8 (2009).
[12] B. Liang, B. Yuan, and J. C. Cheng, Acoustic Diode: Rectification of Acoustic Energy Flux in One-Dimensional Systems, Phys. Rev. Lett. **103**, 104301 (2009).
[13] B. Liang, X. Y. Zou, B. Yuan, and J. C. Cheng, Frequency-dependence of the acoustic rectifying efficiency of an acoustic diode model, Appl. Phys. Lett. **96**, 233511 (2010).
[14] B. Liang, X. S. Guo, J. Tu, D. Zhang, and J. C. Cheng, An acoustic rectifier, Nat. Mater. **9**, 989 (2010).
[15] B. Yuan, B. Liang, J. C. Tao, X. Y. Zou, and J. C. Cheng, Broadband directional acoustic waveguide with high efficiency, Appl. Phys. Lett. **101**, 043503 (2012).
[16] A. L. Song, T. N. Chen, X. P. Wang, and L. L. Wan, Waveform-preserved unidirectional acoustic transmission based on impedance-matched acoustic metasurface and phononic crystal, J. Appl. Phys. **120**, 085106 (2016).
[17] S. Zhang, Y. Zhang, Y. J. Guo, Y. H. Leng, W. Feng, and W. W. Cao, Realization of Subwavelength Asymmetric Acoustic Transmission Based on Low-Frequency Forbidden Transmission, Phys. Rev. Appl. **5**, 034006 (2016).
[18] H. X. Sun, S. Q. Yuan, and S. Y. Zhang, Asymmetric acoustic transmission in multiple frequency bands, Appl. Phys. Lett. **107**, 213505 (2015).
[19] R. Q. Li, B. Liang, Y. Li, W. W. Kan, X. Y. Zou, and J. C. Cheng, Broadband asymmetric acoustic transmission in a gradient-index structure, Appl. Phys. Lett. **101**, 263502 (2012).
[20] Y. F. Zhu, X. Y. Zou, B. Liang, and J. C. Cheng, Broadband unidirectional transmission of sound in unblocked channel, Appl. Phys. Lett. **106**, 173508 (2015).
[21] C. Shen, Y. B. Xie, J. F. Li, S. A. Cummer, and Y. Jing, Asymmetric acoustic transmission through near-zero-index and gradient-index metasurfaces, Appl. Phys. Lett. **108**, 223502 (2016).
[22] X. F. Zhu, H. Ramezani, C. Z. Shi, J. Zhu, and X. Zhang, PT-Symmetric Acoustics, Phys. Rev. X **4**, 031042 (2014).

[23] R. Fleury, D. Sounas, and Andrea Alù, An invisible acoustic sensor based on parity-time symmetry, Nat. Commun. **6**, 5905 (2015).

[24] C. Z. Shi, M. Dubois, Y. Chen, L. Cheng, H. Ramezani, Y. Wang, and X. Zhang, Accessing the exceptional points of parity-time symmetric acoustics, Nat. Commun. **7**, 11110 (2016).

[25] C. Shen, J. F. Li, X. Y. Peng, and S. A. Cummer, Synthetic exceptional points and unidirectional zero reflection in non-Hermitian acoustic systems, Phys. Rev. Mat. **2**, 125203 (2018).

[26] W. W. Zhu, X. S. Fang, D. T. Li, Y. Sun, Y. Li, Y. Jing, and H. Chen, Simultaneous Observation of a Topological Edge State and Exceptional Point in an Open and Non-Hermitian Acoustic System, Phys. Rev. Lett. **121**, 124501 (2018).

[27] J. F. Li, C. Shen, A. Díaz-Rubio, S. A. Tretyakov, and S. A. Cummer, Systematic design and experimental demonstration of bianisotropic metasurfaces for scattering-free manipulation of acoustic wavefronts, Nat. Commun. **9**, 1342 (2018).

[28] J. F. Li, A. Díaz-Rubio, C. Shen, Z. T. Jia, S. A. Tretyakov, and S. A. Cummer, Highly Efficient Generation of Angular Momentum with Cylindrical Bianisotropic Metasurfaces, Phys. Rev. Appl. **11**, 024016 (2019).

[29] S. R. Craig, X. S. Su, A. Norris, and C. Z. Shi, Experimental Realization of Acoustic Bianisotropic Gratings, Phys. Rev. Appl. **11**, 061002 (2019).

[30] T. Liu, X. F. Zhu, F. Chen, S. J. Liang, and J. Zhu, Unidirectional Wave Vector Manipulation in Two-Dimensional Space with an all Passive Acoustic Parity-Time-Symmetric Metamaterials Crystal, Phys. Rev. Lett. **120**, 124502 (2018).

[31] J. P. Xia, X. T. Zhang, H. X. Sun, S. Q. Yuan, J. Qian, and Y. Ge, Broadband Tunable Acoustic Asymmetric Focusing Lens from Dual-layer Metasurfaces, Phys. Rev. Appl. **10**, 014016 (2018).

[32] H. Y. Long, Y. Cheng, and X. J. Liu, Asymmetric absorber with multiband and broadband for low-frequency sound, Appl. Phys. Lett. **111**, 143502 (2017).

[33] H. Y. Long, Y. Cheng, and X. J. Liu, Reconfgurable sound anomalous absorptions in transparent waveguide with modularized multiorder Helmholtz resonator, Sci. Rep. **8**, 15678 (2018).

[34] C. X. Fu, X. N. Zhang, M. Yang, S. W. Xiao, and Z. Yang, Hybrid membrane resonators for multiple frequency asymmetric absorption and reflection in large waveguide, Appl. Phys. Lett. **110**, 021901 (2017).

[35] S. W. Xiao, S. T. Tang, and Z. Yang, Voltage-tunable acoustic metasheet with highly asymmetric surfaces, Appl. Phys. Lett. **111**, 194101 (2017).

[36] Z. W. Zhang, Y. Tian, Y. H. Wang, S. X. Gao, Y. Cheng, X. J. Liu, and J. Christensen, Directional acoustic antennas based on valley-hall topological insulators, Adv. Mat. **30**, 1803229 (2018).

[37] X. C. Wang, A. Díaz-Rubio, V. S. Asadchy, G. Ptitcyn, A. A. Generalov, J. Ala-Laurinaho, and S. A. Tretyakov, Extreme Asymmetry in Metasurfaces via Evanescent Fields Engineering: Angular-Asymmetric Absorption, Phys. Rev. Lett. **121**, 256802 (2018).

[38] M. Yazdi, M. Albooyeh, R. Alaee, V.r Asadchy, N. Komjani, C. Rockstuhl, C. R. Simovski, and S. Tretyakov, A bianisotropic metasurface with resonant asymmetric absorption, IEEE Trans. Antennas Propag. **63**, 3004 (2015).

[39] X. Wang, X. S. Fang, D. X. Mao, Y. Jing, and Y. Li, Extremely asymmetrical acoustic metasurface mirror at the exceptional point, arXiv preprint arXiv:1903.06374, (2019).

[40] T. Lee and H. Iizuka, Acoustic resonance coupling for directional wave control: From angle-dependent absorption to asymmetric transmission, New J. Phys. **21**, 043030 (2019).

[41] C. Shen, A. Díaz-Rubio, J. F. Li, and S. A. Cummer, A surface impedance-based three-channel acoustic metasurface retroreflector, Appl. Phys. Lett. **112**, 183503 (2018).

[42] A. Díaz-Rubio1, J. F. Li, C. Shen, S. A. Cummer, and S. A. Tretyakov, Power flow-conformal metamirrors for engineering wave reflections, Sci. Adv. **5**, 7288 (2019).

[43] A. Díaz-Rubio and S. A. Tretyakov, Acoustic metasurfaces for scattering-free anomalous reflection and refraction, Phys. Rev. B **96**, 125409 (2017).

[44] B. H. Song and J. S. Bolton, A transfer-matrix approach for estimating the characteristic impedance and wave numbers of limp and rigid porous materials, J. Acoust. Soc. Am. **107**, 1131 (2000).

[45] Y. B. Xie, B. I. Popa, L. Zigoneanu, and S. A. Cummer, Measurement of a Broadband Negative Index with Space-Coiling Acoustic Metamaterials, Phys. Rev. Lett. **110**, 175501 (2013).

[46] A. L. Song, J. F. Li, C. Shen, X. Y. Peng, X. H. Zhu, T. N. Chen, and S. A. Cummer, Broadband high-index prism for asymmetric acoustic transmission, Appl. Phys. Lett. **114**, 121902 (2019).

[47] Y. B. Xie, W. Q. Wang, H. Y. Chen, A. Konneker, B.-I. Popa, and S. A. Cummer, Wavefront modulation and subwavelength diffractive acoustics with an acoustic metasurface, Nat. Commun. **5**, 5553 (2014).

[48] M. Amin, O. Siddiqui, W. Orfali, M. Farhat, and A. Khelif, Resonant Beam Steering and Carpet Cloaking Using an Acoustic Transformational Metascreen, Phys. Rev. Appl. **10**, 064030 (2018).

[49] Y. B. Jin, X. S. Fang, Y. Li, and D. Torrent, Engineered Diffraction Gratings for Acoustic Cloaking, Phys. Rev. Appl. **11**, 011004 (2019).